Materials Science in Semiconductor Processing 62 (2017) 80–91

Contents lists available at ScienceDirect

Materials Science in Semiconductor Processing

journal homepage: www.elsevier.com/locate/mssp

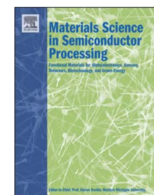

Review article

Laser annealing in Si and Ge: Anomalous physical aspects and modeling approaches

S.F. Lombardo[a,b], S. Boninelli[e], F. Cristiano[c], G. Fisicaro[d], G. Fortunato[a], M.G. Grimaldi[b,e], G. Impellizzeri[e], M. Italia[a], A. Marino[a], R. Milazzo[f], E. Napolitani[f], V. Privitera[e], A. La Magna[a,*]

[a] Istituto per la Microelettronica e Microsistemi (CNR-IMM), VIII Strada 5, 95121 Catania, Italy
[b] Dipartimento di Fisica e Astronomia, Università di Catania, Via Santa Sofia 64, 95125 Catania, Italy
[c] LAAS, CNRS and University of Toulouse, 7 av. Du Col. Roche, 31400 Toulouse, France
[d] University of Basel University of Basel, Klingelbergstrasse 82, CH-4056 Basel, Switzerland
[e] Istituto per la Microelettronica e Microsistemi (CNR-IMM), Via S. Sofia 64, 95123 Catania, Italy
[f] CNR-IMM MATIS and Dipartimento di Fisica Astronomia, Università di Padova, Via Marzolo 8, 35131 Padova, Italy

ARTICLE INFO

Keywords:
Laser Annealing
Phase field modeling
Non equilibrium diffusion

ABSTRACT

Laser annealing of semiconductor materials is a processing technique offering interesting application features when intense, transient and localized heat sources are needed for electronic device manufacturing or other nano-technological applications. The space-time localization of the induced thermal field (in the nanoseconds/nanometers scale) promotes interesting non-equilibrium phenomena in the processed material which only recently have been systematically investigated and modelled. In this review paper we discuss the current knowledge on anomalous kinetics occurring in implanted silicon and germanium (i.e. thin layers of disorder diluted alloys of Si and Ge, with variable initial disorder status according to the implantation conditions) during the pulsed laser irradiation. In particular, we focus our attention on the anomalous impurity redistribution in the transient melting stage and on the formation of non conventional and metastable extended defects.

1. Introduction

Laser Annealing (LA) is the preferred material processing option when heating of extremely localized regions of the specimen is required. The possible applications include all the micro- and nano-fabrications in which a local material modification needs to be activated at high temperature (T) while this thermal budget could be detrimental for the materials and structures present in the surroundings areas. In the semiconductor technologies the importance of LA increases with the complexity of the realized/proposed integration schemes. Indeed, its use is often proposed when, in complex integration schemes, additional device structures have to be built on top of pre-fabricated ones, which have to be shielded by the subsequent fabrication processes of the new structures. A non exhaustive list of these device architectures includes: backside junctions and metallization in vertical power devices, thin film displays, high frequency bipolar silicon on glass processes, CMOS backside images or 3D integration (see Ref. [1] for a complete discussion on LA applications in emerging technologies).

In many of these applications LA is preceded by a process (e.g. impurity implantation or low temperature deposition) producing a strongly disordered or amorphous material. Moreover, for the majority of the proposed conditions, LA induces localized melting and the ultra fast recovery of the crystalline order. As a consequence, the far from equilibrium kinetics is a key aspect of the material modifications caused by LA. In addition, non-equilibrium phenomena are often exploited to obtain the desired results: e.g. the non-equilibrium impurity segregation during the fast solidification favours the incorporation of high concentrations of electrically active dopant atoms [2–4].

Recently systematic studies by means of accurate and correlated chemical-physical and micro-structural analyses of samples processed by LA in different conditions have revealed a series of anomalous aspects, which cannot be fully and correctly described by the previous theoretical and modeling assessment. The anomalies concern many of the post-process physical observables: the alloy redistribution [5–8], the electrical activation of ion-implanted impurities [9–11], the defect evolution [12–14], the observation of non-conventional extended defects [1,15]. The particular focus of this paper is the current theoretical understanding of the LA results in terms of the micro-structural and atomistic ultra rapid evolution of the processed systems. We restrict our analysis on systems based on the two most popular semiconductors, namely silicon (Si) and germanium (Ge), materials of importance for nano-electronic applications; however, most of the

* Corresponding author.
E-mail address: antonino.lamagna@imm.cnr.it (A. La Magna).

http://dx.doi.org/10.1016/j.mssp.2016.10.047
Received 23 August 2016; Received in revised form 20 October 2016; Accepted 27 October 2016
Available online 07 November 2016
1369-8001/ © 2016 Elsevier Ltd. All rights reserved.

arguments here discussed can also impact the theoretical comprehension of the non-equilibrium kinetics in other systems.

The plan of the paper is the following: in section 2 the necessary theoretical background for the simulation of the LA process is presented, section 3 focuses on anomalies of the alloy redistribution during rapid melting and solidification provoked by LA, in section 4 the results of LA induced kinetics at sub-μs time scale in damaged semiconductors are discussed, finally section 5 reports some conclusive remarks.

2. Theoretical background

With respect to other processing techniques, e.g. a conventional thermal process, LA in some sense maximizes the interaction between equipment and specimen. Indeed, if we consider the laser-beam as part of the equipment, the driving force for the material modification depends strongly on the sample's geometry and material type, due to the impact of the laser light diffraction and thermal diffusion within the irradiated structures [3,16,4]. Any accurate modeling of the microstructural kinetics during LA cannot be developed regardless of a precise determination of the thermal field and the eventual melting front kinetics. In this section we will discuss this necessary preliminary simulation formalism based on electromagnetic calculations coupled with a phase field model for the evolving temperature and phase fields.

2.1. Electromagnetic calculations for the heat sources in laser-annealing

In laser annealing, using pulsed laser configurations, the spatial distribution of the electromagnetic (e.m.) power can be considered uniform over areas ~cm ^{2}. The coherence length L_c of the e.m. field is in general much smaller than the pulse dimension $L_c \ll 1$ cm but much larger than the feature size (e.g. the pitch $\sim 10^{-8} - 10^{-7}$ cm, for the case of a periodic pattern of devices) of the irradiated structures. As a consequence, we can assume that the heat source is generated by a generic incident "coherent" electromagnetic plane wave with fixed angular frequency ω in a given polarization state. The laser pulse is usually specified in terms of the total fluence (energy density) E_{laser} in $[J \times \mathrm{cm}^{-2}]$ units and the normalized power density $P_{norm}(t)$

$$\int_0^{\Delta t_{pulse}} P_{norm}(t)dt = 1 \tag{1}$$

where $P_{norm}(t) \equiv 0$ when $t < 0$ or $t > \Delta t$. The pulse duration Δt_{pulse} is usually much larger than the inverse of the frequency

$$\nu^{-1} = \left(\frac{\omega}{2\pi}\right)^{-1} = \left(\frac{c}{\lambda}\right)^{-1}, \tag{2}$$

where ω is the angular frequency and c is the light speed. For example for a laser wave length $\lambda = 308 \times 10^{-9}$ m the inverse of the frequency is $\nu^{-1} = 308 \times 10^{-9}/299792458 \sim 10^{-15}$ s while the usual range of Δt_{pulse} is $20 - 200 \times 10^{-9}$ s. These considerations make ineffective any fully time dependent solution of the Maxwell equations for the heat source calculations in the case of the LA problem under study. An "adiabatic-like" formulation of the heating problem is necessary assuming that the change of the optical constants during the annealing is slow with respect the system response to the electromagnetic excitation. In this approximation, with the additional assumption that the electromagnetic excitation is efficiently transferred from the electrons to the photons (see ref. [13] for a complete discussion on this issue) we can determine the heat sources using stationary (or time harmonic) evaluation of the resistive heat averaging the "ultra-fast" time scales of the oscillating electromagnetic field

$$S_{laser}(t, \mathbf{r}) = \frac{\varepsilon''}{2\rho}|\mathbf{E}^{th}(\mathbf{r})|^2 \cdot P_{norm}(t) \tag{3}$$

Where ε'' is the imaginary part of the complex dielectric constant $\varepsilon = \varepsilon' + j\varepsilon''$ of the material and $\mathbf{E}^{th}$ is the time harmonic electric field $\mathbf{E} = \mathbf{E}^{th} \times exp(-j\omega t + \phi)$ that can be evaluated by the following time independent form (i.e. the time harmonic Maxwell curl-curl problem)

$$\nabla \times (\boldsymbol{\mu}^{-1}\nabla \times \mathbf{E}^{th}) - j\omega(\sigma - j\omega\boldsymbol{\epsilon})\mathbf{E}^{th} = j\omega\mathbf{J}, \quad in\ \Omega \tag{4}$$

and

$$\mathbf{n} \times \mathbf{E}^{th} = \mathbf{n} \times \mathbf{E}_{\mathbf{0}}^{th}, \quad on\ \partial\Omega_e \tag{5}$$

$$\mathbf{n} \times (\boldsymbol{\mu}^{-1}\nabla \times \mathbf{E}^{th}) + j\omega\mathbf{n} \times (\lambda(\mathbf{n} \times \mathbf{E}^{th})) = j\omega\mathbf{J}_f + j\omega\mathbf{n} \times \mathbf{H}_0, \quad on\ \partial\Omega_h \tag{6}$$

where

$$\partial\Omega = \partial\Omega_e \cap \partial\Omega_h \tag{7}$$

and

$$\partial\Omega_e \cup \partial\Omega_h = 0 \tag{8}$$

here $\Omega \subset \mathbb{R}^d (d\ is\ the\ system\ dimension)$ is an open, bounded domain with boundary $\Gamma = \partial\Omega$, $\partial\Omega_e$ ($\partial\Omega_h$) is a boundary where a condition on the electric (magnetic) field is imposed, $\mathbf{J} \in (L^2(\Omega))^d$ is a given vector function indicating the internal source and $\omega \in \mathbb{R}(\omega \neq 0)\mathbf{n}$, is the unit outward normal vector to $\partial\Omega$.

For a Transversal Electrical (TE) mode and in the absence of internal sources

$$\mathbf{E}^{th} = E_z^{th}\mathbf{z} \tag{9}$$

$$\frac{\partial E_z^{th}}{\partial z} = 0 \tag{10}$$

and Eq. (5) takes the form of the Helmotz equation

$$-\nabla(\boldsymbol{\mu}^{-1}\nabla E_z^{th}) - j\omega(\boldsymbol{\sigma} - j\omega\boldsymbol{\epsilon})E_z^{th} = 0 \tag{11}$$

and

$$E_z^{th} = E_0^{th} \quad on\ \partial\Omega_e \tag{12}$$

$$-\mathbf{n}\cdot\nabla E_z^{th} - jkE_z^{th} = +j\omega\mathbf{n} \times \mathbf{H_0}. \quad on\ \partial\Omega_h \tag{13}$$

Since the optical parameters depend significantly on temperature and phase, Eqs. (3) and (11) have to be solved self-consistently with the phase and temperature evolution equations (see the following subsection) to evaluate the time and space dependent heat sources.

2.2. Phase field formalism

Accurate simulations of the temperature and phase evolution due to heat generation by means of pulsed irradiation can be achieved within the phase field formalism [4], which in addition permits a natural integration of evolution models for other quantities of interest (e.g. impurities, defects). The phase field model is an ideal framework for studying phase transition problems, because it allows simulating the evolution in time and space of the phase boundary without the explicit tracking of the boundary itself. These results are achieved using a phase field variable ψ which varies with continuity from one phase to another. An accurate mathematical model derivation, including extended analytical and numerical tests, can be found in the seminal work of Karma and Rappel (K-R) [17] based on the following phase field equations for a generic temperature T driven solid-liquid phase transition:

$$\tau\frac{\partial\psi}{\partial t} = W^2\nabla^2\psi - \frac{\partial F(\psi, \lambda u)}{\partial\psi} \tag{14}$$

$$\frac{\partial u}{\partial t} = D_T\nabla^2 u + \frac{1}{2}\frac{\partial h(\psi)}{\partial t} \tag{15}$$

where

$$F(\psi, \lambda u) = f(\psi) + \lambda g(\psi)u \tag{16}$$

and

$$u = \frac{c_p(T - T_M)}{L} \tag{17}$$

The following parameters are introduced: W is the (finite) width of the liquid-solid interface, D_T is the heat diffusivity c_P the constant pressure specific heat and L the latent heat. Here $F(\psi, \lambda u)$ and h must be chosen in a way that the diffuse interface solutions coincide with the free boundary problem in the sharp interface limit.

$$\frac{\partial u}{\partial t} = D_T \nabla^2 u V = D_T(\partial_n u|^- - \partial_n u|^+) u_i = -\frac{d_0}{R} - \beta V \tag{18}$$

where d_0 is the capillarity length and β is the kinetic coefficient which relates the local interface temperature T_i to the local interface speed. K-R propose a double well function with minima at $\phi = -1$ (liquid) and $\phi = +1$ (solid) using the following expressions for f, g, h

$$f(\psi) = -\frac{\psi^2}{2} + \frac{\psi^4}{4} \tag{19}$$

$$g(\psi) = \psi - \frac{2\psi^3}{3} + \frac{\psi^5}{5} \tag{20}$$

$$h(\psi) = \frac{15}{8}\left[\psi - \frac{2\psi^3}{3} + \frac{\psi^5}{5}\right] \tag{21}$$

where the variational choice $h(\psi) \propto g(\psi)$ and the additional constraint

$$\frac{h(+1) - h(-1)}{2} = 1 \tag{22}$$

are imposed in order to guarantee that the correct amount of latent heat is produced/consumed at the moving interface. The sharp interface limit fixes the λ value in Eq. (16) as the one satisfying the following equation

$$\beta = a_1\left[\frac{\tau}{\lambda W} - a_2\frac{W}{D_T}\right] \tag{23}$$

with $a_1 = 0.8839$ and $a_2 = 0.3981$ while $d_0 = a_1 W/\lambda$ [17]. Please note that a non linear relation between $V(T_i)$ and the moving interface temperature u_i (e.g. Fulcher-Vogel type expressions [3]) can be easily implemented deriving a function $\lambda[V(T_i)]$ from $\beta[V(T_i)]$ with the use of the expression (23).

Thus, the explicit forms of Eqs. (14) and (15) are

$$\tau\frac{\partial \psi}{\partial t} = W^2\nabla^2\psi - \frac{\partial f}{\partial \psi} - \lambda u\frac{\partial g}{\partial \psi} = W^2\nabla^2\psi + \psi(1-\psi)(1+\psi) - \lambda u(1-\psi)^2(1+\psi)^2 \tag{24}$$

and

$$\frac{\partial u}{\partial t} = D_T\nabla^2 u + \frac{1}{2}\frac{\partial h(\psi)}{\partial t} = D_T\nabla^2 u + \frac{15}{16}(1-\psi)^2(1-\psi)^2\frac{\partial \psi}{\partial t} \tag{25}$$

or for the absolute temperature T

$$c_p\frac{\partial T}{\partial t} = K\nabla^2 T + L\frac{15}{16}(1-\psi)^2(1-\psi)^2\frac{\partial \psi}{\partial t} \tag{26}$$

where K is the heat conductivity. Equivalent phase field formulations can be found in the literature, which can be derived from the K-R one by means of transformation of the phase function. For example the phase field formalism of Wheeler et al. [2,18] practically coincides to the K-R one when the transformation

$$\phi = \frac{\psi + 1}{2} \tag{27}$$

is performed in the previous equations. We obtain

$$-\frac{\partial f}{\partial \psi} = 4\phi(1-2\phi)(1-\phi) = -\frac{\partial \tilde{f}}{\partial \phi} \tag{28}$$

$$-\frac{\partial g}{\partial \psi} = -16\phi^2(1-\phi)^2 = -\frac{\partial \tilde{g}}{\partial \phi} \tag{29}$$

$$\frac{1}{2}\frac{\partial h(\psi)}{\partial t} = 30\phi^2(1-\phi)^2\frac{\partial \phi}{\partial t} = \frac{1}{2}\frac{\partial \tilde{h}(\phi)}{\partial t} \tag{30}$$

and

$$2\tau\frac{\partial \phi}{\partial t} = 2W^2\nabla^2\phi - \frac{\partial \tilde{f}}{\partial \phi} - \lambda u\frac{\partial \tilde{g}}{\partial \phi} \tag{31}$$

$$c_p\frac{\partial T}{\partial t} = D\nabla^2 T + L\frac{1}{2}\frac{\partial \tilde{h}(\phi)}{\partial t} \tag{32}$$

which represents a phase field formulation which starts from a free energy density of the form

$$\tilde{f}(\phi) = -\phi^2(1-\phi)^2 \tag{33}$$

and

$$\tilde{g}(\phi) = 8\left(\frac{1}{3}\phi^3 - \frac{1}{2}\phi^4 + \frac{1}{5}\phi^5\right) \tag{34}$$

3. Anomalous impurity redistribution during a melting LA process

Ultra fast melting and subsequent solidification, induced by pulsed laser irradiation of ion implanted semiconductor samples, promote concurrent non-equilibrium phenomena leading to a significant modification of the micro-state of these systems. In particular: the implantation damage is healed if the melting involves the whole implanted region, impurities redistribute due to the high diffusivity in the liquid state, the rapid crystallization traps a high density of impurities in (active) substitutional crystal sites. Although, this complex kinetic evolution has been consistently modelled in several cases, integrating diffusion-segregation models in the phase field formalism [3,18], the diffuse impurity chemical and active profiles show systematic anomalies needing additional theoretical development and formalism refinements. In this section all these issues will be discussed.

3.1. Non equilibrium impurity trapping

The kinetic states of diluted alloys in solid and liquid phases are completely different, whereas thermal fluctuations promote long range migration in the liquid phase whilst vibrations and related activated short range jumps rule atom redistribution in the solid phase. As a consequence the impurity diffusion coefficient jumps many orders of magnitude (e.g. from $D_l \sim 10^{-4}$ to $D_s \sim 10^{-12}$ cm^2/s) from the liquid to the solid regions of an evolving solid-liquid system. The two phases are in contact during a solidification phenomenon and the solid-liquid interface marks a boundary between these regions where atoms dynamically transit between these two kinetic states, and the local alloy (impurity) density changes at the two sides of the interface. As a consequence a fundamental parameter is the partition coefficient k^P defined as the ratio between the impurity density $k^p = c_s/c_l$ at the two sides of the interface. As we will discuss in the following k^P can strongly depend on the particular solidification evolution; however, in quasi-equilibrium conditions for an ideally dilute alloy the partition coefficient assumes a constant value $k^p \longrightarrow k_e^p$ which can be derived from the phase diagram of the binary system under study in the $c \longrightarrow 0$ region (see Fig. 1). For the case of negative derivatives of the liquidus and solidus lines, which is the typical situation of doped Si and Ge samples, a less then unity $k_e^p < 1$ is obtained.

In the case of solidification which ends at a particular boundary (e.g. the material surface or the interface with a solid material with higher melting point), the combined effect of the high diffusivity in the

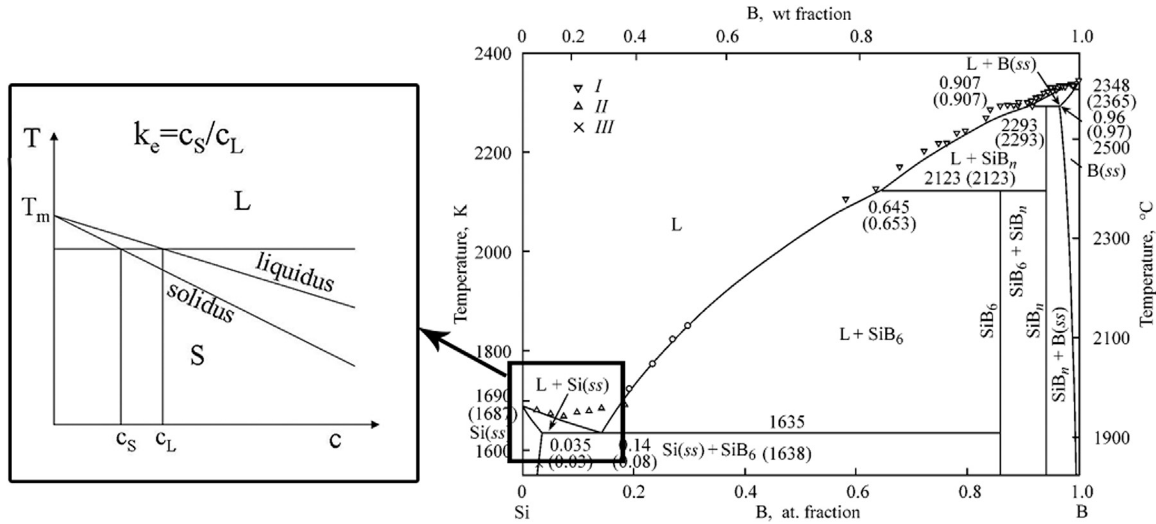

Fig. 1. Derivation of the equilibrium partition coefficient from the phase diagram for a dilute alloy. The phase diagram for the Boron-Silicon alloy is shown in the right panel whilst a schematic for generic alloy is zoomed in the left panel. Solid, Liquid and coexistence regions are indicated and separated by the liquidus and solidus lines. For an under-cooling temperature close to the melting point $T < T_m$ and slow regrowth speed v_{ls}, $k^P{}_e$ is the constant maximum ratio between the densities at the solid and liquid sides of the interface. Russian Journal of General Chemistry, Thermodynamic Properties and Phase Equilibria in the Si-B System, 72, 2002, A. I. Zaitsev, with permission of Springer.

liquid region and the $k^p < 1$ value of the partition coefficient is the progressive accumulation of the impurity close to the boundary (i.e. the formation of the so called segregation peak). Assuming the quasi-equilibrium condition we could model this dopant redistribution using a Fick-like diffusion model with a moving boundary

$$\frac{\partial c}{\partial t} = D_s \nabla^2 c \quad in \quad \Omega_{solid} \tag{35}$$

$$\frac{\partial c}{\partial t} = D_l \nabla^2 c \quad in \quad \Omega_{liquid} \tag{36}$$

$$c = c_s = k_e^p c_l \quad on \quad \partial\Omega_{solid} \quad c = c_l \quad on \quad \partial\Omega_{liquid} \tag{37}$$

Where Ω_{solid} and Ω_{liquid} are the solid and liquid domains while $\partial\Omega_{solid}$ and $\partial\Omega_{liquid}$ are their evolving internal boundaries whose evolution can be, for example, simulated by means the phase field model.

The limiting case is the redistribution of marker atoms of the same substrate, e.g. implanted ^{30}Si in ^{28}Si substrate [19], in this case $k_e^p = 1$ is expected.

The LA processes for the case of laser pulses in the range of 10^{-7} s or less induce solidification speeds of the order of fews m/s which are away from the quasi-equilibrium conditions. In this case the impurity trapping phenomenon occurs, which causes a more efficient incorporation of the impurity in the solid semiconductor lattice with respect the equilibrium limit given by k_e^p. This phenomenon has been systematically studied experimentally [20–25] and consistently modelled by means of Kinetic Lattice Monte Carlo (KLMC) simulations of the solidification in the canonical statistical *ensamble* at an under-cooling condition $\Delta T_{u-c} = T_i - T_m$ with $T_i < T_m$ [26].

This method simulates the solidification as a statistical sequence of Monte Carlo events occurring at the solid-liquid interface where atoms transit from the liquid phase (i.e. a L-site) to the solid one (i.e. an S-Site of the lattice under study) and vice-versa. The “actual” transition is stochastically selected in the list of “possible” transitions according to its own probability ruled by a bond counting energetic. Consequently the transition probability of a solid to liquid event is [26]

$$P_{SL} = P_0 \times \exp[-n_S(\Phi_s - \Phi_l)/k_B T], \tag{38}$$

where n_S is the number of bonds which the interface site forms with atoms in the solid phase, Φ_s is the bond energy when the bond is formed by two atoms in the solid phase and Φ_l is the bond energy when one of the two atoms forming the bond is in the liquid phase. Similarly, the transition probability of a liquid to solid event is

$$P_{LS} = P_0 \times \exp[-\Delta S_B/k_B] \tag{39}$$

where $\Delta S_B/k_B = 2(\Phi_s - \Phi_l)/k_B T_m$ is the entropy of fusion and T_m is the melting point. For a silicon crystal T_m=1688. The value of bond difference for Si is $\Phi_s^{Si-Si} - \Phi_l^{Si-Si} = 0.96\,eV$ [27], while the probability pre-factor is calibrated by correlating the simulated interface speed with the experimental interface speed $V_{sl}(T)$ as a function of temperature (i.e. the undercooling) [28].

In order to study non-equilibrium trapping, Φ_s values have to be calibrated for the binary system under investigation in order to consider the Si-Si (or Ge-Ge) bond Φ_s^{Si-Si}, the Si-X impurity bond Φ_s^{Si-X} and the impurity-impurity bond Φ_s^{X-X} [29]. The impurity diffusion in the liquid region can be considered by means of a random jump sequence where the jump frequency is derived from the known diffusivity values of X in the liquid phase.

A snapshot of a KLMC simulation, obtained after $t \sim 8\,ns$ of simulated evolution of an under-cooled partially-molten Si system, (T=1660 K) is shown in Fig. 2 for an impurity parametrized by $k_e^p = 0.05$ and $D_l = 2.\ 10^{-4}$ (similar values are obtained by impurities like In or Sb in Si). Impurities accumulate in the liquid region as effect of the segregation and analyzing the simulation the effective partition coefficient $k^p[V_{sl}(T)]$ ($V_{sl}(T = 1660\ K) \sim 3\ m/s$ in Si) can be calculated by the average ratio of the impurity density levels estimated by the KLMC simulations at the solid and liquid sides of the interface.

Calibrated KLMC simulations give reliably the non-equilibrium impurity trapping effect in a good agreement with the known experimental data [20]. The calculated partition coefficient $k[V_{sl}(T)]$ is shown in Fig. 3 for three different impurities in Si (please note the β variable reported in Fig. 3 is an adimensional parameter proportional to $V_{sl}(T)$). It is worth to note that $k[V_{sl}(T)]$ monotonically increases with the interface speed starting from the equilibrium value $k_e^p = k[V_{sl}(T \simeq T_M) \simeq 0]$ and asymptotically reaches the limit value $k[V_{sl}(T) \gg 1 m/s] = 1$.

3.2. Phase field models of impurity trapping and full LA simulations

Phase field models show a strong potential for the accurate simulation of the non-equilibrium solute trapping. The reference formalism has been developed in the papers of Ahmad et al. [18] and specifically applied to the complete simulation of LA processes of Si and Ge implanted samples in the papers of La Magna and co-workers [3,4,10]. The progressive reduction in the impurity (solute) density change across the interface as the solidification rate increases, beyond the value predicted by equilibrium thermodynamics, is not included as

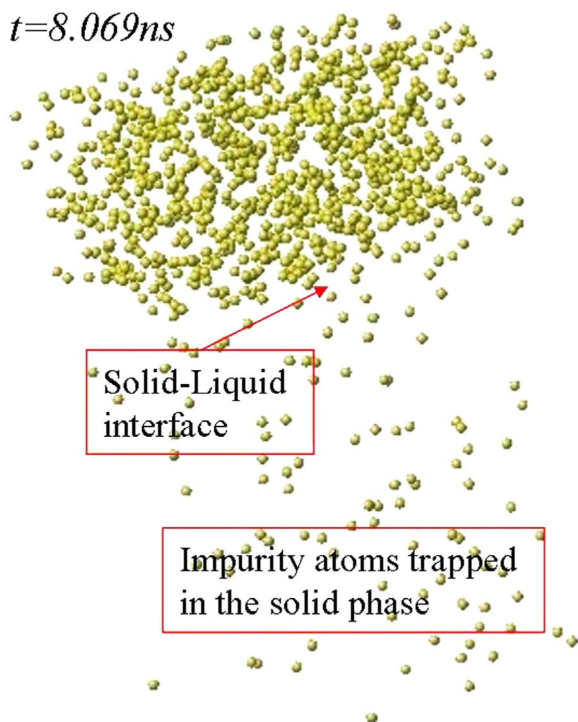

Fig. 2. Snapshot of simulated KLMC evolution of the re-growth of a doped Si system at T=1660 K. Only impurity atoms are shown.

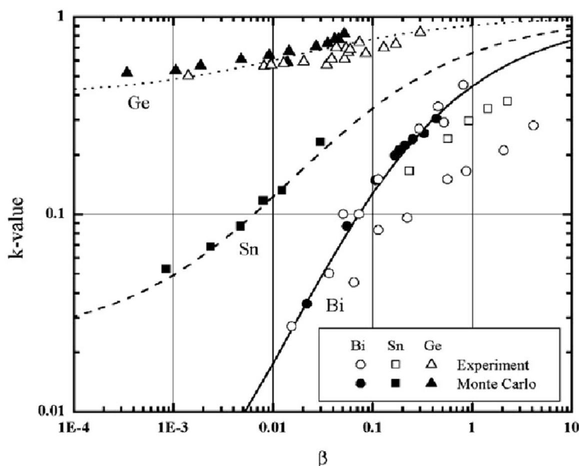

Fig. 3. Effective partition coefficient in Si for various impurities as a function of the solidification speed: KLMC results and experimental data. Reprinted from Journal of Crystal Growth, 264, Kenneth A. Jackson, Constitutional supercooling surface roughening, 519–529, 2004, with permission from Elsevier.

an external calibration as in the case of the traditional sharp-interface description (see Eqs. (18) and (35)) with $k[V_{sl}(T)]$ instead of k_e^p. Indeed, the trapping is recovered directly by the model's solutions whereas its parameters are $k^p{}_e$ and the impurity diffusivity as a function of ϕ and T. Moreover, the formalism also considers the energy dissipation in the phase boundary region resulting in a solute drag [18].

Following the derivation of Ref. [18] we can extend the Eq. (33) in the case of a dilute solid solution of a dopant X in the host substrate S, as a linear superposition of the two terms, F_S and F_X, related to the two species plus a term related to entropy of mixing, i.e [2]:

$$F(\phi, T, c) = (1-c)F_S(\phi, T) + cF_X(\phi, T) + + \frac{kT}{v_m}[c\ln c + (1-c)\ln(1-c)], \tag{40}$$

where v_m is the solvent (substrate) molecular volume. This term produces a further variational equation for the impurity density c which adds to the phase field model [18]:

$$\frac{\partial c}{\partial t} = \nabla\left[M_2 c(1-c)\nabla\frac{\delta F}{\delta c}\right]. \tag{41}$$

where the positive parameter M_2 is related to the interface and solute mobility. After a proper rescaling of the microscopic parameters in terms of the thermodynamical ones, the following diffusion-segregation equation is derived for the impurity density

$$\frac{\partial c}{\partial t} = \nabla[D(\phi, T)\nabla c] - D(\phi, T)\ln(k_e^p)\nabla[c(1-c)d(\phi)\nabla\phi], \tag{42}$$

where $d(\phi) \propto \delta f/\delta\phi$ is related to the specific phase field functional used and $D(\Phi, T)$ is the phase and temperature diffusivity [30,31]. The diffusivity functional satisfies the obvious constraint $D(\Phi = \Phi_{solid}, T) = D_s(T)$ and $D(\Phi = \Phi_{liquid}, T) = D_l(T)$ and its dependency on the phase rules the non equilibrium segregation behaviour [3,18].

In Fig. 4 an example of phase field simulation results in Si are shown for a ~30 ns laser pulse (simulation and experimental details are reported in Ref. [3]) and compared with experimental profiles measured by Secondary Ion Mass Spectrometry (SIMS). The initial system is an implanted Si (As at 30 keV 7° tilt, 30° twist angles to a dose of 10^{15} ions/cm^2) with uniform $T = T_{in}$=450 °C ($k_e^p = 0.3$ for As in Si).

The simulations reveal the liquid-solid boundary evolution with a varying speed depending on the driving space and time dependent thermal field [3]. During melting, the impurity redistribution is ruled by the large diffusivity in the liquid phase and by the boundary motion which limit the diffusion (impurities practically do not diffuse in the solid phase during the process). In the regrowth stage (the s-l interface speed V_{sl} is $\sim 2\ m/s$ in this case) the non-equilibrium segregation phenomenon, which determines the impurity density incorporated into the solid phase. Since the $c_s/c_l < 1$ the simulated profiles show a peak at the surface (see Fig. 4). Anyhow, due to the non-equilibrium trapping, the impurity density accumulating at the surface is significantly smaller when compared with that obtained by simulations reproducing quasi-equilibrium conditions ($V_{sl} \sim 0$ and $c_s/c_l = 0.3$) [3].

3.3. Anomalous redistribution of impurities in group IV elements in melting LA processes

In the last decades ultra shallow junctions (e.g. junction depth ≤50 nm) in semiconductors have been fabricated and experimentally

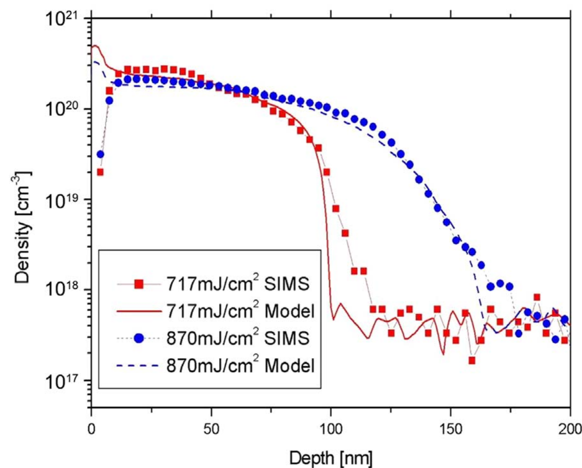

Fig. 4. As profiles after single pulse LA processes in the case of a ~30 ns wide laser pulse. SIMS profiles points and (thin lines) simulated profiles (thick lines). The density peaks at the surface due to the non-equilibrium segregation cannot be observed in the experimental profiles due to the resolution limit of SIMS (~10 nm) close the surface. Data from La Magna et al. Ref. [3].

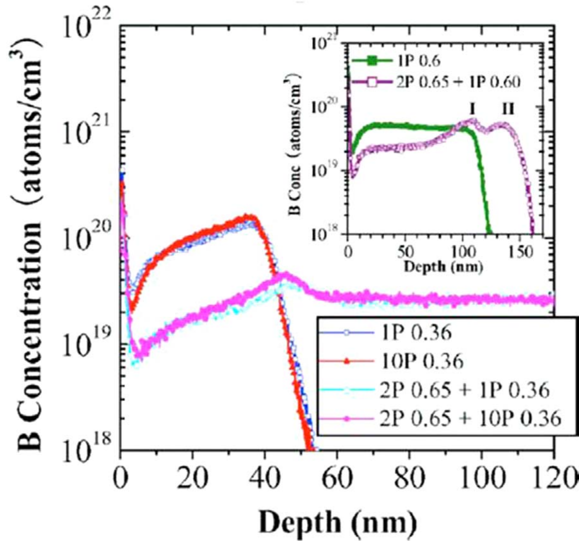

Fig. 5. Example of ultra shallow boron profiles measured by SIMS obtained by LA in the melting regime of low energy implants of B in Si. Anomalous peaks at the maximum depth are observed. Reprinted from Ong, Pey, Lee, et al., Dopant distribution in the recrystallization transient at the maximum melt depth induced by laser annealing, Appl. Phys. Lett. 89, 172111 (2006), with the permission of AIP Publishing.

analyzed in view of the possible application as a manufacturing process of scaled nano-electronic devices. This research has revealed diffusion-segregation phenomena which cannot be understood using the non-equilibrium kinetic theory for dilute alloys discussed in the previous subsection. In particular, anomalous peaks close to melt depth region (see for example Fig. 5) are systematically observed in shallow profiles of implanted Si-X and Ge-X (X=B, P and As) alloys after LA [32,33,6,8]. Comparing the shapes of simulation profiles in Fig. 4 and the ones in Fig. 5, we can conclude that the observed effects cannot be revealed by the non-equilibrium trapping theory. Indeed, even when the limit value of $k^p \longrightarrow 1$ is achieved, the eventual result is the absence of segregation peaks at the surface (see e.g. the green solid line obtained using k^p=1, which can be compared to the experimental profile in Fig. 6).

Phenomenological models have been proposed [33,34] to fit experimental data. They are based on transient "boundary free" dependence for k^p to be determined by fitting the profile. Within these models k^p takes the equilibrium value k_e^p at the very beginning of the crystal re-growth, then increases to a fitting value $k_{trans}^p > 1$ in a transient stage and then achieves a value $k_p < 1$ in the last stage of the solidification until the solidification is completed.

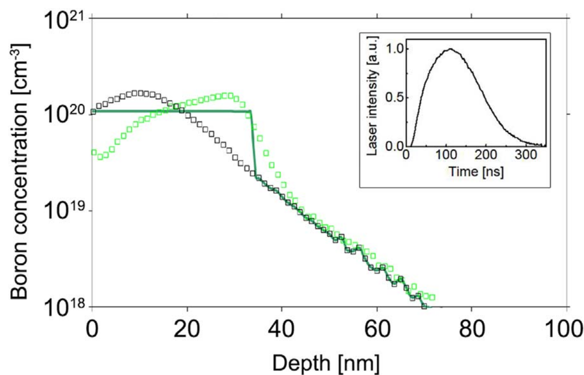

Fig. 6. SIMS (green squares) B profiles obtained after a post-implantation (as implanted is shown as black squares) laser irradiation at 2.0 J/cm^2. Simulation profile assuming k^p=1 is shown as thick green lines. In the inset the laser pulse is plotted. Data from Fisicaro et al. Ref. ([5]). (For interpretation of the references to color in this figure legend, the reader is referred to the web version of this article.)

Actually, this phenomenological description, based on $k^p > 1$ for alloys with $k_e^p < 1$ contradicts the non-equilibrium segregation models discussed in 3.1, which in turn have been developed in a general framework of the theory of the non equilibrium phenomena and, in addition, are consistent with the KLMC atomistic simulations. In particular, Kaplan et al. [35] have demonstrated that the so called continuum growth model [20,36] (giving the limit behaviour of $k^p \longrightarrow 1$ for $V \longrightarrow \infty$ with boundaries $k_e^p \leq k^p < 1$) satisfies the Onsager's reciprocity relations [37,38] for the irreversible processes. $k^p > 1$ for an alloy with $k_e^p < 1$ implies an effective inversion of the solidus and liquidus lines in the original equilibrium phase diagram (see Fig. 1), which is difficult to derive in the framework of the theory of the irreversible processes.

An alternative model has been proposed in the ref. [5], which does not involve the segregation behaviour at the solid-liquid boundary and derives the anomalous redistribution of the impurities as an indirect effect of their diffusion mechanism in the liquid semiconductor. The underlying assumption on the basis of this diffusion mechanism is the presence of two states, with proper bonding configuration, for the solute atoms dissolved in the liquid semiconductor. These states, characterized by strongly different mobilities, are in a dynamic equilibrium ruled by the local temperature.

The presence of more bonding configurations of the impurities is correlated to the atomic structures of l-Si and l-Ge [39–41] showing a mixed and fluctuating covalent + metallic bonding characters: The state with low (high) diffusivity should locally trigger the formation of covalent (metallic) bonds for the surrounding Si atoms. The balance of these two components of the solute density gives rise to a globally non-fickian diffusion of impurities in l-Si(Ge) which, as we are going to discuss, explains their anomalous redistribution. The diffusion model is formulated in terms of the following equations [5]:

$$\frac{\partial c}{\partial t} = \frac{\partial c^{HD}}{\partial t} + \frac{\partial c^{LD}}{\partial t} \tag{43}$$

$$\frac{\partial c^{HD}}{\partial t} = \nabla[D^{HD}\nabla c^{HD}] + k^{\tau}(c^{LD} - \overline{R}\cdot c^{HD}) \tag{44}$$

$$\frac{\partial c^{LD}}{\partial t} = \nabla[D^{LD}\nabla c^{LD}] - k^{\tau}(c^{LD} - \overline{R}\cdot c^{HD}) \tag{45}$$

where D^{HD} and D^{LD} are the impurity diffusivity in the higher and lower diffusivity state in liquid phase. c^{HD} and c^{LD} are the corresponding concentrations. $\overline{R}(T)$ is the average (equilibrium) ratio between low and high diffusivity states at constant T. Please note that for non-equilibrium processes the temperature in the liquid phase is not, in general, restricted to $T > T_m$. Molecular Dynamics simulations of ref. [41] have demonstrated that a covalent bond component in l-Si prevails in the under-cooled liquid state and causes a strong reduction of the l-Si self-diffusion. Consistently we can deduce that impurity atoms in the lower diffusivity state dominate the migration in under-cooled regions and $\overline{R}(T) > 1$, whilst $\overline{R}(T) < 1$ for T well above the melting point and atoms in the higher diffusivity state characterize the impurity kinetics. In the solid phase metallic bonds are not present and $D_{sol} = D_{sol}^{HD} = D_{sol}^{LD}$ [30]. k^{τ} is a rate coefficient controlling the transition between the two states which should be also related to the rapidity of the bonding order fluctuations in l-Si and l-Ge. Its value has been generally fixed as a constant [5,6], although a T dependence can be derived when additional data will be available for more refined estimates of the model parameters.

Fig. 7 for the 2.3 J/cm^2 laser fluence case (the pulse is shown in the inset of Fig. 6), shows in detail how pile-up close to the maximum melt depth region could arise from the diffusion model of Eqs. (43)–(45). The simulation starts from the as implanted B profile in Si of Fig. 6 (B 3 keV energy, 5×10^{14} cm^{-2} dose, black circles in the figures).

The temperature field (Fig. 7 green solid line) identifies under-cooled and non-undercooled regions of l-Si and helps in the different

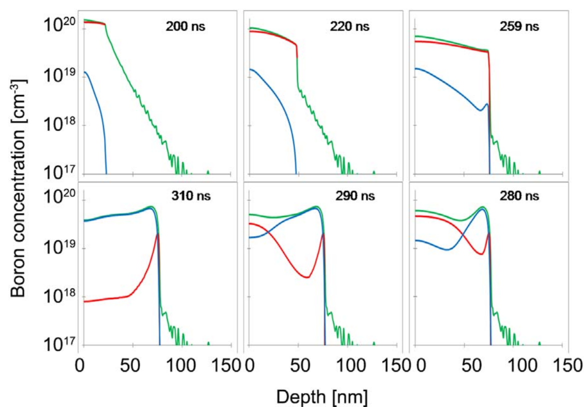

Fig. 7. Dopant evolution during the laser irradiation processing (2.3 J/cm^2). The time after the start of the pulse is indicated for each snapshot. Plots in the upper (lower) panel refer to the melting (re-growth) stage. The boron concentration is indicated by the green line, the HD and the LD components by the red and blue lines respectively. Data from Fisicaro et al. ref. ([5]). (For interpretation of the references to color in this figure legend, the reader is referred to the web version of this article.).

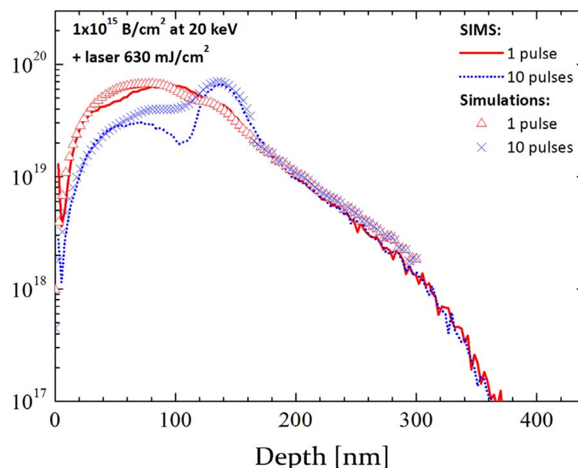

Fig. 9. Implanted boron profile in Ge (10^{15} B/cm^2 at 20 keV) after LA (630 mJ/cm^2) for 1 (red continuous line) and 10 pulses (blue dotted line). B profiles simulated with the two state model are also reported (1 pulse red triangle, 10 pulses blue crosses. Data from Impellizzeri et al. ref. [6]. (For interpretation of the references to color in this figure legend, the reader is referred to the web version of this article.)

evolution stages. Dopant atoms in the lower diffusivity state are strongly favoured in regions with $T < T_m$ whilst atoms in the higher diffusivity state characterize the impurity kinetics in the stable liquid regions. For the laser irradiation conditions considered the melt depth is greater than the dopant region and during the melting stage (upper panels of Fig. 7) the majority of the dopant atoms (71%) reside in their high diffusivity state as the temperature is significantly above the Si melting point. During re-growth the dopant atoms are shifted towards the solid/liquid interface (lower panels of Fig. 7, blue lines), due to the presence of the under-cooled phase which favours the B state with low diffusivity and a large density gradient of the high diffusivity component (red lines). As a consequence a net migration of impurity atoms from left to right (in the panel) is the combined result of the two-component evolution which causes the pile-up. Temperature-dependent diffusivity in the liquid phase is an obvious consequence of the two-state model. However, the anomalous redistribution is an additional effect being the impurity pile-up mechanism inherently related to the local un-balance between states with high and low mobility.

Comparisons between the model's prediction of diffusion profiles and B density profiles measured by SIMS in implanted Si (B 3 keV energy, 5×10^{14} cm^{-2} dose, black circles in the figures) after single pulse LA processes at different energy densities are shown in Fig. 8. The post-LA B profiles predicted by the diffusion model (solid lines in Fig. 8) are in satisfying agreement with the experimental ones. A similar agreement between theoretical predictions and experimental profiles is revealed for the multi-pulse case when a saturation of the pile-up tendency is observed (for a detailed discussion see Ref. [5]).

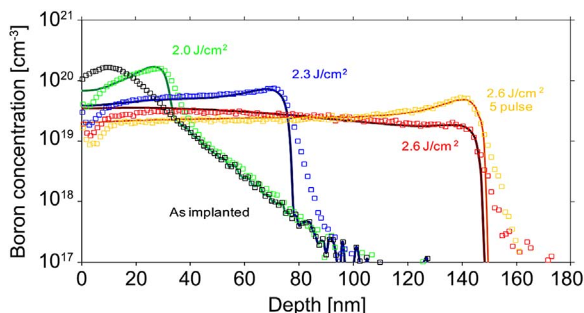

Fig. 8. SIMS (squares) and simulated (by means of the two-state model Eqs. (43)–(45), solid lines) B profiles obtained after single pulse laser irradiations at 2.0 (green), 2.3 (blue), and 2.6 (red) J/cm^2 energy densities. Multi-pulse case (5 pulses) is shown as orange curves. The value of $k^{\tau} = 1.0 \times 10^7 [s^{-1}]$ is used. Data from Fisicaro et al. ref. ([5]). (For interpretation of the references to color in this figure legend, the reader is referred to the web version of this article.)

The high temperature value used in the simulation $\overline{R}(T) = 0.4$ for $T \gg T_m$ is very similar to the ratio of covalent/metallic bonds ~0.42 in l-Si calculated by Štich et al. [39] by means of Car-Parrinello molecular dynamics simulations of molten Si. The *l*-Si boron diffusivity in the high (low) diffusivity state was found to be $D_B^{HD} = 3.3 \times 10^{-4}$[cm^2/s] ($D_B^{LD} = 6.6 \times 10^{-5}$[cm^2/s]). Note that the experimental value of the B diffusivity in the stable non-undercooled *l*-Si D = 2.4×10^{-4} cm^2/s [31] is revealed by the two-state model in the case of a uniform ratio of the two components.

As already stated, pile-up after LA occurs also in implanted Ge as shown by the SIMS profile after LA from the analysis of Fig. 9, where post-LA B profiles in Ge are plotted. In this case the dopant redistribution is also affected by the tendency of B atoms to aggregate, not considered in the model, due to the low solubility of B in *l*-Ge, which also contributes to pile-up formation and peculiar profile shape. The B cluster formation in *l*-Ge explains the difference between simulated and measured profiles.

4. Activation, ripening-less large defect formation and non conventional I loops

Segregation and impurity trapping phenomena during re-crystallization induced by LA lead to an almost ideal solid solution of impurities in Si and Ge, where solute atoms are located in active sites. As a consequence, for a melting LA process the activation mechanism is tightly related to these phenomena. However, LA is also interesting for applications where melting is not induced or where both melting and high temperatures are applied to process the samples. A typical example of the latter application is the formation of p-n junctions where implanted impurities closer to the surface are activated by segregation from the liquid phase whilst impurities with opposite charge state implanted in depth are activated by the thermal budget [9]. During a thermal annealing process, solid phase activation of implanted impurities is the result of the complex evolution, at atomic level, of the defects (generated by the implantation) and the impurities. In the past decades the interaction between defects and dopant atoms in semiconductor substrates has attracted an intense research effort; and, for the case of conventional thermal processes (uniform temperature, ~*s* process duration), the transient phenomena (including diffusion) [42] controlled by the defect-impurity kinetics have been satisfyingly understood and accurately modelled [43]. In particular, the defect stability and their atomic structure as a function of the size have been deeply investigated since defect clusters and extended defects of

different morphologies characterize the evolution of the implantation damage and its interaction with the impurity field, whereas the growth of larger defect aggregates occurs at the expenses of the smaller ones (Ostwald ripening) and is the main underlying mechanism of this evolution [44,45].

This experimental and theoretical assessment cannot be easily extended when the thermal process is induced by sub-μs laser irradiation, since huge thermal gradients and ultra fast heating/quenching drive the defect-impurity system to strongly dynamic and non equilibrium conditions. In order to highlight with a single example the differences, we note that a remarkable effect of the laser localized and transient annealing is the dopant activation without diffusion in the solid phase [32,33,9], whilst activation after the transient enhanced diffusion is the characteristic phenomenon in the case of conventional annealing [42].

In this section we review the results of recent studies on the ultra fast kinetics of the defect-impurity systems in semiconductor induced by LA.

4.1. Extension of the kinetic monte carlo method to full la processes

The kinetic Monte Carlo (KMC) method permits the accurate simulation of the kinetics in defect-impurity systems at the mesoscopic scale for long annealing time and uniform temperature [44,45]. An extension of this method has been applied for the simulation of LA processes, characterized by highly non-uniform thermal fields (temperature typically drops by a hundred degrees over a few tens of nanometers) as well as by phase changes when melting takes place [12,46]. A key feature of this method is the coupling of the cited KMC formalism with the phase field model (PF-KMC) which predicts the temperature and phase evolution in irradiated samples, where the main modification of the KMC approach is the occurrence of local event rates

$$\nu = \nu_0 \times e^{-E(\phi)/kT} \tag{46}$$

where $E(\phi)$ is the activation energy, while the temperature and phase $T(t, \mathbf{r})$, $\phi(t\ \mathbf{r})$ are space and time dependent variables.

The Monte Carlo particles are Interstitial- (I) and Vacancy (V)-type defects (point defects and aggregates), dopant atoms residing in a substitutional (i.e. active) position X_s and their complexes with defects, i.e. dopant-interstitial and dopant-vacancy clusters [47]. According the usual KMC assumptions the mobile particles are the I and V point defects as well as the XI and XV complexes (one dopant atom bounded to one I or V point defect), while defect clusters I_m and V_m as well as the dopant-defect cluster X_nI_m X_nV_m (a cluster formed by n dopant atoms and m defects) can only absorb or emit mobile particles [43]. The Monte Carlo event table is represented by the following chemical-like reactions:

$$I + V \leftrightarrow 0 \tag{47}$$

$$I + I_m \leftrightarrow I_{m+1} \tag{48}$$

$$V + V_m \leftrightarrow V_{m+1} \tag{49}$$

$$I + V_m \leftrightarrow V_{m-1} \tag{50}$$

$$V + I_m \leftrightarrow I_{m-1} \tag{51}$$

$$I + X_s \leftrightarrow XI \tag{52}$$

$$V + X_s \leftrightarrow XV \tag{53}$$

$$I + X_nI_m \leftrightarrow X_nI_{m+1} \tag{54}$$

$$V + X_nV_m \leftrightarrow X_nV_{m+1} \tag{55}$$

$$V + X_nI_m \leftrightarrow X_nI_{m-1} \tag{56}$$

$$I + X_nV_m \leftrightarrow X_nV_{m-1} \tag{57}$$

$$XI + X_nI_m \leftrightarrow X_{n+1}I_{m+1}. \tag{58}$$

$$XV + X_nV_m \leftrightarrow X_{n+1}V_{m+1}. \tag{59}$$

$$XV + X_nI_m \leftrightarrow X_{n+1}I_{m-1}. \tag{60}$$

$$XI + X_nV_m \leftrightarrow X_{n+1}V_{m-1}. \tag{61}$$

X_n complexes can eventually form and annihilate only through the interaction with the mobile particles. The parameter calibration should extend the assessment on migration and complex energetics [47,45,48–50,43,51] applied with success in the case of conventional annealing to temperatures close to the melting point. The case of the B in Si is presented and critically discussed in Refs. [12,46] (in this case vacancy-impurity complexes are unstable). In the liquid state free and clustered defects annihilate whilst dopant atoms are formally positioned in a substitutional state X_s in the liquid phase and during the segregation.

In Fig. 10 is an example of PF-KMC simulation for two possible choices of the calibration parameters (the pulse is shown in Fig. 6, whilst a detailed discussion is reported in Ref. [12]). The analysis focuses on the residual I-type defect after a melting LA process. It is noteworthy that a relatively high density of residual defects after the process is predicted by the PF-KMC simulations. Moreover, the results show a cluster size distribution limited to the small size region (the density of cluster with size larger than 10 I is negligible) for this sub-μs irradiation process. A residual high local density of V-type defects is also evidenced by the simulation [12]. We would like to mention that KMC approaches, implementing similar calibration parameters for the event rates, predict the formation of extended defects for the case of conventional thermal annealing [43].

4.2. Diffusion less activation in solid phase during LA processes: the B-Si system

Impurity diffusion in the solid phase is negligible for sub-μs LA processes and only activation (i.e. the local modification of electrochemical potential) shows a relevant dynamics [32,33,9,52]. The PF-KMC method presented in the previous subsection could simulate the activation dynamics, computing the portion of the dopant chemical profile (not showing diffusion) corresponding to substitutional impurities X_s. In Figs. 11 and 12 examples of these simulation results are

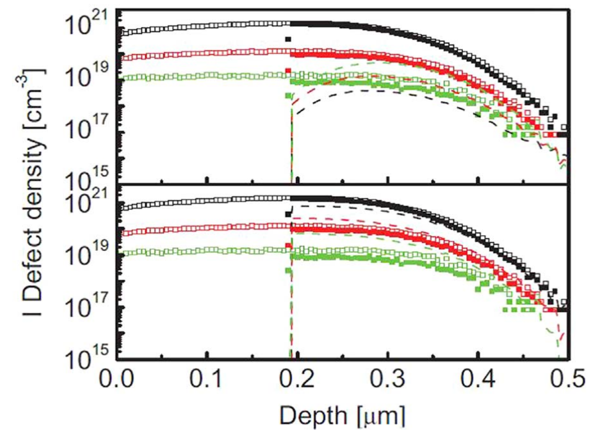

Fig. 10. Simulated interstitial density in implanted Si (P energy 200 keV and dose of 10^{14} cm^{-2}) after room temperature evolution during implantation (empty squares) and one-pulse (filled squares) laser irradiation of 2.6 J/cm^2 laser fluence obtained by means of the KMC code. Dashed lines refer to PDE simulation for the same process carried out with two different calibration for the cluster dissolution rates. Dark, red (dark gray), and green (light gray) lines refer, respectively, to distributions of clusters formed by two, three, and four defects. Reprinted figure with permission from Fisicaro et al., APS Physical Review E, 86, 2012. Copyright 2016 by the American Physical Society. (For interpretation of the references to color in this figure legend, the reader is referred to the web version of this article.)

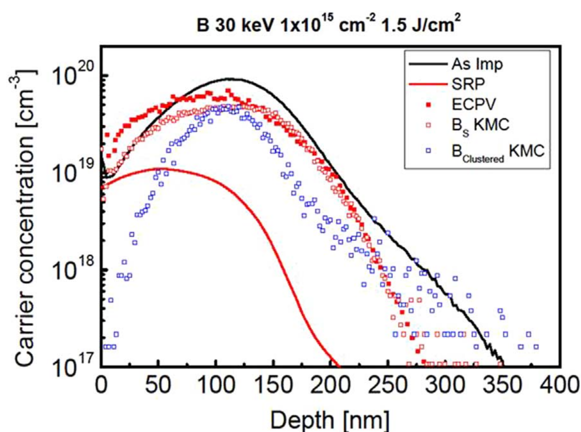

Fig. 11. Activated boron profile measured by Spreading Resistance Probe (red solid line) and electrochemical capacitancevoltage (red filled squares) in post-implanted Si samples (B 30 keV energy dose of 10^{15} cm^{-2} as implanted profile is the black line) after a one pulse laser process at 1.5 J/cm^2 laser fluences. Empty red squares refer to the simulated substitutional boron atoms, while empty blue squares are simulated boron atoms in boron interstitial cluster. Data from Fisicaro et al. ref. [46]. (For interpretation of the references to color in this figure legend, the reader is referred to the web version of this article.)

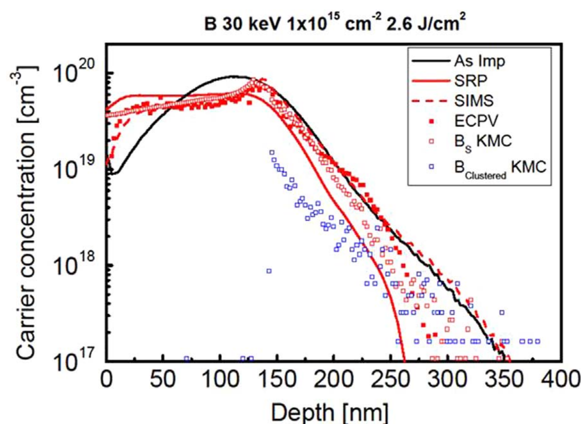

Fig. 12. Activated boron profile measured by Spreading Resistance Probe (red solid line) and electrochemical capacitance voltage (red filled squares) in post-implanted Si samples (B 30 keV energy dose of 10^{15} cm^{-2} as implanted profile is the black line) after a one pulse laser process at 2.6 J/cm^2 laser fluences. Empty red squares refer to the simulated substitutional boron atoms, while empty blue squares are simulated boron atoms in boron interstitial cluster. Data from Fisicaro et al. ref. [46]. (For interpretation of the references to color in this figure legend, the reader is referred to the web version of this article.)

shown (again for the laser pulse in Fig. 6) for a non melting and partial melting process of B implants (30 keV energy, 1×10^{15} cm^{-2} dose, projected range $R_p \sim 120\,nm$) in Si respectively (a full description of the methodology is reported in Ref. [46]). Initial state of the impurity-defect system after the implant is calculated by means of coupled KMC +Binary Collision Approximation (BCA) simulations at room temperature [12].

The heat released by the irradiation in the solid phase causes a local displacement of boron atoms in substitutional lattice sites as well as the formation of immobile aggregates with interstitial defects (i.e. BICs). Moreover, transient thermal budget activates the aggregates' dissolution which increases the overall activation by means of the inverse reaction of Eq. (52).

Figs. 11 and 12 report the boron component stored in the B_nI_m clusters for all the cited laser irradiation conditions. The maximum melt depth (evidenced by the anomalous segregation peak) is about 150 nm. Comparing the B_s and B_nI_m densities in regions ($z > 150\,nm$) where the samples remain solid for both the 1.5 to the 2.6 J/cm^2 cases, we can observe a pronounced decrease of the local density of BICs with the increase of the laser fluence and the related thermal budget. Anyhow, a saturation of the local activation efficiency has been observed in the melting process with the increase in fluence [46]. Moreover, the PF-KMC code shows also a rapid activation saturation with the increase of the shot number (not shown here, see ref. [46] for the details) in agreement with the experimental analysis. These results indicate that the formation of stable boron-interstitial aggregates limits the solid-phase activation efficiency during the laser-induced kinetics in the presence of a highly-damaged crystalline matrix. Similar large local density of defects and similar I cluster size distribution as that reported in Fig. 10 is obtained in this case.

Simulation results are compared in Figs. 11 and 12 for validation with experimental chemical (SIMS) and electrically active profiles. Chemical B profiles have been analyzed by means of SIMS, while the electrical activation has been evaluated experimentally both on a qualified SSM150 spreading resistance profiling (SRP) system and a electrochemical capacitance-voltage (ECV) equipment. In general the simulation predictions are correctly validated by the experimental analysis (especially for the ECV results) which demonstrates significant activation levels are reached in all annealing conditions. The discrepancy between the activation levels extracted by means of the ECV and SRP for the non melting case has been explained considering the measurement peculiarities in the presence of a highly defective matrix [46].

The satisfying results of the PF-KMC method for the particular non equilibrium condition provoked by LA could suggest that the theoretical framework of defect-impurity system kinetics is substantially correct. We would like to outline the main assumptions of this framework: a) separated channels for the I-type and V-type defects which interact only by annihilation reactions (see Eqs. (47)–(61)), b) Ostwald-type ripening mediated by monomer diffusion and driven by the stability of larger defect aggregates with respect of smaller ones, c) no significant role of the structural rearrangement in different complex morphologies (e.g. small cluster, 311-type defects, dislocation loops; see [53] for a critical discussion on this issue) during the ripening phenomenon, d) high stability of small defect-impurity complexes. A direct extension of this scenario is assumed in the PF-KMC method (with the relevant modification of the inclusion of local temperature and phase) and the same calibration carried out for uniform temperature annealing is used. PF-KMC simulates activation in agreement with experiments as the result of competitive events: namely dissolution/capture events of the mobile BI from/by a B_nI_m complex and its diffusion in the highly damaged crystalline matrix before being promoted in to the B_s state by the I release. Anyhow, stark differences between theoretical and experimental scenarios emerge when microstructure of the defect system are analyzed by transmission electron microscopy (TEM) as we will discuss in the next subsection.

4.3. Ripening-less formation of large (001) I loops during LA

PF-KMC simulations indicate that a highly damaged crystal should emerge after LA processes of implanted semiconductor samples in a non melting condition. According to the implemented model scheme, the damage is represented by a huge density of point defects and small defect clusters; moreover a strongly incomplete annihilation of the I and V components is predicted. Impurities are activated by the irradiation but the activation efficiency is strongly influenced by the co-presence of the defects.

The microstate of this highly damaged crystal can be experimentally characterized by advanced microscopy techniques. Fig. 13 shows results obtained by Atom probe tomography (APT) for the same sample (processed at 2.6 J/cm^2 fluence) whose activation is analyzed in Fig. 12. The APT measurements are performed in a selected volume below the melt depth (i.e. in the region where solid phase activation occurs). No large B-only clusters or loops decorated by B atoms are evidenced by the APT. However, the quantitative statistical method

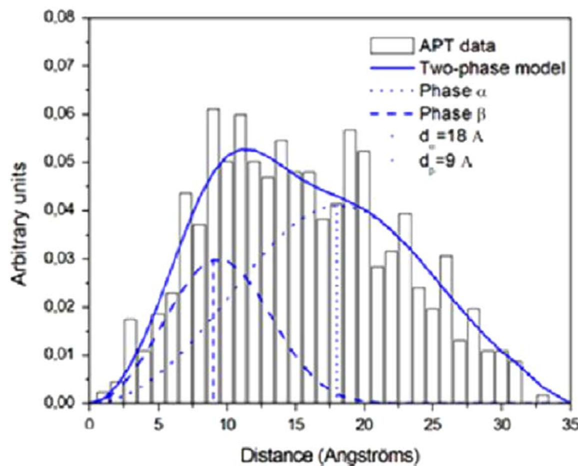

Fig. 13. Distribution of the first nearest neighbor (1NN) distances between B atoms measured by atom probe tomography (APT) analysis in a volume below the melt depth of the boron implanted Si sample (B 30 keV energy dose of 10^{15} cm^{-2}) annealed with 2.6 J/cm^2. The distribution is fitted with a two phase model (solid line). Dotted and dashed lines represent the distributions related to the solid solution cluster phases, respectively. Reprinted with permission from Y. Qiu, F. Cristiano, K. Huet, et al., Extended Defects Formation in Nanosecond Laser-Annealed Ion Implanted Silicon, Nano letters, 14, 1769–1775 2014. Copyright 2016 American Chemical Society.

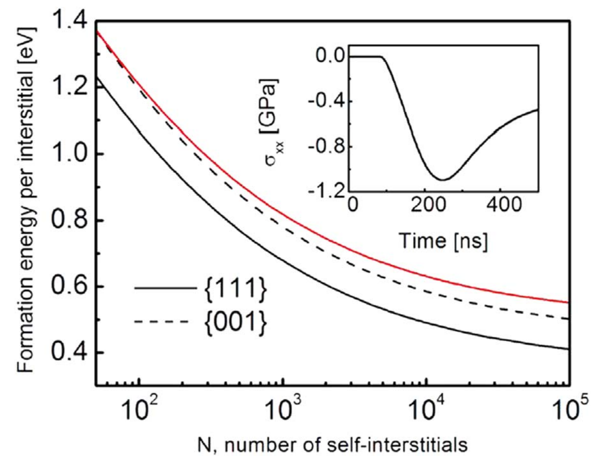

Fig. 15. Inset: Stress variation as a function of annealing time calculated at a depth of 100 nm for a laser annealing at a temperature just below the melting threshold. A maximum biaxial compressive stress of 1 GPa is estimated after 200 ns. Main plot: Formation energy of {111} and (001) dislocation loops as a function of defect size in the absence of an external stress (black curves) and in the presence of the calculated stress induced by LA. The energy of (001) loops does not change when biaxial stress is applied. Reprinted with permission from Y. Qiu, F. Cristiano, K. Huet, et al., Extended Defects Formation in Nanosecond Laser-Annealed Ion Implanted Silicon, Nano letters, 14, 1769–1775 2014. Copyright 2016 American Chemical Society.

applied to the distance distribution between the first nearest neighbor atoms reveals that boron atoms are not in a perfect solid phase solution, indicating that there is a clustering trend and the ratio between the clustered and free component are in a reasonable agreement with the PF-KMC results reported in Fig. 12.

In spite of this evidence, which is consistent with the presence of a clustered component of B trapped in small BICs as the PF-KMC simulations predict, the TEM analysis using weak-beam dark-field (WBDF) imaging conditions clearly shows that I-type defects are instead large I-type loops containing thousands of interstitials [15]. These loops are not related to the boron presence, as the results reported Fig. 14 obtained after Si^+ implantation demonstrate. Here implantation conditions are chosen to generate similar initial damage as the B^+ implants. The fact that the residual damage after the LA process is dominated by extended defects is not the only peculiar finding. Even more surprising is the atomic structure of these defects, since WBDF-TEM indicate that the vast majority of defects (almost 100% for the sample in Fig. 14) consist of (001) dislocation loops (DLs) instead of the conventional and well studied I-type loop with {111} Burgers vector. High Resolution TEM (HRTEM) images (see the inset in 14) of an area containing a loop seen with its habit plane being perpendicular to the image plane clearly show that the defect consists of an additional plane of atoms parallel to the (001) plane.

{111} I-type dislocation loops are extremely stable and are ubiquitously recovered as the final stage of the Ostwald ripening process of interstitial defects in Si during the conventional thermal process. Moreover, their formation energy is significantly smaller than the formation energy of the (001) loops as is shown in Fig. 15. As a consequence the occurrence of (001) DLs is not expected as the result of rearrangement of the I-type defects in stable aggregates.

An explanation of this result has been proposed in terms of the inversion of the relative stability of the two classes of loops in the presence of external stress [1,15]. Indeed, the damaged region is subjected during the irradiation to a relevant transient biaxial stress in the xy plane parallel to the surface as a consequence of the high temperature gradients provoked by the irradiation. The inset of Fig. 15 shows the stress variation as a function of annealing time calculated at a depth of 100 nm for the case of a Si sample irradiated at 1.5 J/cm^2 (the pulse is shown in Fig. 6). This transient stress is calculated by means of the linear thermo-elastic theory based on the fast varying thermal field computed by the phase field model [15]. A maximum compressive stress σ_{xx} or σ_{yy} ~1 GPa is evaluated after 200 ns. The biaxial compressive stress does not modify the formation energy of (001) loops since their Burgers vectors are perpendicular to the stress plane. In contrast, the formation energy of {111} DLs increases under the applied stress. Fig. 15 shows as a red line, the modification of the formation energy of the conventional {111} DLs calculated at the time of maximum compressive stress. For this stress value the formation energy of {111} loops overcomes that of (001) loops, which should become under these transient conditions the most stable extended I-defect configurations.

This argument based on energetic considerations is a plausible explanation of the experimental results. However, the ultra rapid evolution of the implantation damage that leads to the formation of

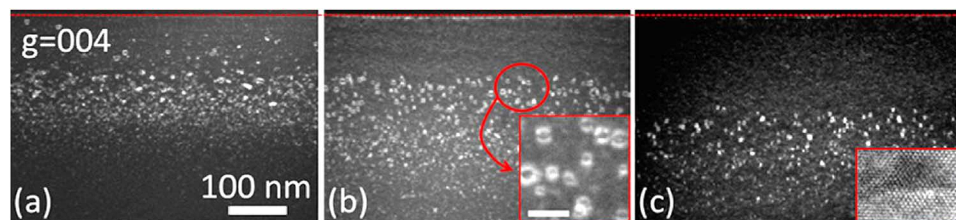

Fig. 14. Cross section TEM images (surfaces are indicated by the red dashed line) of the Si^+ implanted Si sample annealed by (a) 10 pulses at 1.5 J/cm^2 (non melting case), (b) 1 pulse at 2.6 J/cm^2 (partial melting case above the projected range of the implantation). Scale bar in the inset is 20 nm, (c) 1 pulse at 2.9 J/cm^2 (melting case below the projected range of the implantation). Inset: HREM image of a loop with (001) habit plane. Reprinted with permission from Y. Qiu, F. Cristiano, K. Huet, et al., Extended Defects Formation in Nanosecond Laser-Annealed Ion Implanted Silicon, Nano letters, 14, 1769–1775 2014. Copyright 2016 American Chemical Society.

this extended defect is still puzzling. Indeed, as PF-KMC simulations demonstrate they cannot be formed by means of a diffusion mediated Ostwald ripening process which causes a gradual increase of the aggregates' average size. Moreover, the successful description of the ripening phenomenon for I-type defects in conventional annealing processes (i.e. ~s time scale) is based on an initial state (i.e. the so called +1 model where the *I* density profile coincides with the implanted impurity profile) emerging after the early stage of the annealing, whereas the details of the evolution in this early stage are not relevant at long annealing times. In contrast, in a sub-μs LA process we should carefully describe at atomic level the ultra rapid evolution of the defect-impurity system. As a consequence even the KMC scheme (where free defects and defect aggregates are separated objects with fixed structure which depend only on the size) could be insufficient to achieve accuracy for this atomic level kinetics. Indeed, whilst the predicted high total density of residual defects after LA is probably correct (see Fig. 11), the formation mechanism of the observed extended defects could be inaccessible to the PF-KMC formalism.

Preliminary results obtained with Molecular Dynamics simulations [54] indicate that highly damaged Si could locally evolve in to (001) loop configurations in the nanoseconds time scale, where the formation of stable loops is preceded by a pseudo-amorphous stage. This ripening-less mechanism is qualitatively in agreement with the experimental scenario. However further experimental and theoretical investigations are necessary to fully explain the results discussed here.

5. Conclusion

In this paper we present the current understanding of a difficult investigation subject: i.e. the kinetics of a disordered alloy induced by transient (in the sub μs time scale) thermal field generated by pulsed irradiation. In contrast to the study of system evolution at larger time scale, intermediate stages cannot be experimentally analyzed and this aspect is maybe the main difficulty in achieving this understanding. Anyhow, the microstate of as prepared and post-processed systems can be characterized in detail with advanced measurement techniques and modeling can, in principle, cover missing knowledge.

We have tried to demonstrate that the systematic investigations performed in the past ten years have raised issues with the previous assessment in the case of two important topics: a) the non-equilibrium alloy segregation phenomenon, b) the mechanism which stabilizes impurities and crystal damage in the sub μs time scale. This fact is not surprising since this assessment was achieved for less extreme non-equilibrium conditions. The controversial experimental findings discussed here are:

- the anomalous pile up of the solute in the melting process induced by sub μs LA;
- the diffusion-less activation dynamics during LA;
- the ultra fast formation of extended defects;
- the stabilization of non conventional extended defects.

All the related observations are difficult to categorize using the schemes used in the case of conventional thermal processes. We have also discussed the complexity of the modeling techniques which have to be implemented to simulate quantitatively the kinetics during LA processes. Indeed, even the basic computational framework requires a coupled Maxwell and phase field solver with parameters well calibrated in a broad range of thermodynamic conditions. The model extensions proposed to explain these findings are based, in general, on a more accurate description of the system microstate. The modeling development is not definitive and still improvements are necessary in terms of completeness of the theoretical framework and accuracy of the parameter calibration. Several open questions have been clearly indicated which could be hints and guidelines for future investigations.

Acknowledgement

This work is partially supported by the cooperation project between CNR and CNRS “Understanding and Modeling of Excimer Laser Annealing” (UMEX).

References

[1] F. Cristiano, M. Shayesteh, R. Duffy, K. Huet, F. Mazzamuto, Y. Qiu, M. Quillec, H. Henrichsen, P. Nielsen, D. Petersen, A. L. Magna, G. Caruso, S. Boninelli, Defect evolution and dopant activation in laser annealed si and ge, Materials Science in Semiconductor Processing 42, Part 2 (2016) 188–195, e-MRS Spring Meeting 2015 Symposium Z: Nanomaterials and processes for advanced semiconductor {CMOS} devices http://dx.doi.org/10.1016/j.mssp.2015.09.011 URL ⟨http://www.sciencedirect.com/science/article/pii/S136980011530189X⟩

[2] A.A. Wheeler, W.J. Boettinger, G.B. McFadden, Phase-field model for isothermal phase transitions in binary alloys, Phys. Rev. A 45 (1992) 7424–7439. http://dx.doi.org/10.1103/PhysRevA.45.7424 (URL ⟨http://link.aps.org/doi/10.1103/PhysRevA.45.7424⟩).

[3] A. La Magna, P. Alippi, V. Privitera, G. Fortunato, M. Camalleri, B. Svensson, A phase-field approach to the simulation of the excimer laser annealing process in si, J. Appl. Phys. 95 (9).

[4] A. La Magna, P. Alippi, V. Privitera, G. Fortunato, Role of light scattering in excimer laser annealing of si, Appl. Phys. Lett. 86 (16) http://dx.doi.org/10.1063/1.1906318 URL ⟨http://scitation.aip.org/content/aip/journal/apl/86/16/10.1063/1.1906318⟩.

[5] G. Fisicaro, K. Huet, R. Negru, M. Hackenberg, P. Pichler, N. Taleb, A. La Magna, Anomalous impurity segregation and local bonding fluctuation in l-si, Phys. Rev. Lett. 110 (2013) 117801. http://dx.doi.org/10.1103/PhysRevLett.110.117801.

[6] G. Impellizzeri, E. Napolitani, S. Boninelli, G. Fisicaro, M. Cuscun, R. Milazzo, A.L. Magna, G. Fortunato, F. Priolo, V. Privitera, B-doping in ge by excimer laser annealing, J. Appl. Phys. 113 (11). http://dx.doi.org/10.1063/1.4795268 URL ⟨http://scitation.aip.org/content/aip/journal/jap/113/11/10.1063/1.4795268⟩

[7] E. Bruno, G.G. Scapellato, A. La Magna, M. Cuscun, E. Napolitani, S. Boninelli, F. Priolo, G. Fortunato, V. Privitera, Anomalous transport of sb in laser irradiated ge, Appl. Phys. Lett. 101 (17).http://dx.doi.org/10.1063/1.4764069 URL ⟨http://scitation.aip.org/content/aip/journal/apl/101/17/10.1063/1.4764069⟩

[8] R. Milazzo, E. Napolitani, G. Impellizzeri, G. Fisicaro, S. Boninelli, M. Cuscun, D. De Salvador, M. Mastromatteo, M. Italia, A. La Magna, G. Fortunato, F. Priolo, V. Privitera, A. Carnera, N-type doping of ge by as implantation and excimer laser annealing, J. Appl. Phys. 115 (5). http://dx.doi.org/10.1063/1.4863779 URL ⟨http://scitation.aip.org/content/aip/journal/jap/115/5/10.1063/1.4863779⟩

[9] K. Huet, G. Fisicaro, J. Venturini, H. Besaucle, A. La Magna, Defect kinetics and dopant activation in submicrosecond laser thermal processes, Appl. Phys. Lett. 95 (23). http://dx.doi.org/10.1063/1.3268472 URL ⟨http://scitation.aip.org/content/aip/journal/apl/95/23/10.1063/1.3268472⟩

[10] G. Fisicaro, A.L. Magna, G. Piccitto, V. Privitera, Laser annealing of sige and ge based devices, Microelectronic Engineering 88 (4) (2011) 488–491, post-Si-CMOS electronic devices: the role of Ge and III-V materials. http://dx.doi.org/10.1016/j.mee.2010.09.014 URL ⟨http://www.sciencedirect.com/science/article/pii/S0167931710003473⟩

[11] G. Fisicaro, L. Pelaz, M. Aboy, P. Lopez, M. Italia, K. Huet, F. Cristiano, Z. Essa, Q. Yang, E. Bedel-Pereira, M. Quillec, A.L. Magna, Kinetic monte carlo simulations of boron activation in implanted si under laser thermal annealing, Appl. Phys. Express 7 (2) (2014) 021301 (URL ⟨http://stacks.iop.org/1882-0786/7/i=2/a=021301⟩).

[12] G. Fisicaro, L. Pelaz, P. Lopez, A. La Magna, Kinetic monte carlo simulations for transient thermal fields: computational methodology and application to the submicrosecond laser processes in implanted silicon, Phys. Rev. E 86 (2012) 036705. http://dx.doi.org/10.1103/PhysRevE.86.036705.

[13] G. Fisicaro, A. La Magna, Modeling of laser annealing, J. Comput. Electron. 13 (1) (2014) 70–94. http://dx.doi.org/10.1007/s10825-013-0545-9.

[14] R. Milazzo, G. Impellizzeri, D. Piccinotti, A. La Magna, G. Fortunato, D. De Salvador, A. Carnera, A. Portavoce, D. Mangelinck, V. Privitera, E. Napolitani, Impurity and defect interactions during laser thermal annealing in ge, J. Appl.Phys. 119 (4). http://dx.doi.org/10.1063/1.4940737 URL ⟨http://scitation.aip.org/content/aip/journal/jap/119/4/10.1063/1.4940737⟩

[15] Y. Qiu, F. Cristiano, K. Huet, F. Mazzamuto, G. Fisicaro, A.L. Magna, M. Quillec, N. Cherkashin, H. Wang, S. Duguay, D. Blavette, Extended defects formation in nanosecond laser-annealed ion implanted silicon, Nano Lett. 14 (4) (2014) 1769–1775. http://dx.doi.org/10.1021/nl4042438 (pMID: 24588318).

[16] A.La Magna, P. Alippi, V. Privitera, S. Scalese, S. Pannitteri, G. Fortunato, L. Mariucci, M. Camalleri, Material modifications induced by laser annealing in two-dimensional structures, Appl. Phys. Lett. 84 (23).

[17] A. Karma, W.-J. Rappel, Quantitative phase-field modeling of dendritic growth in two and three dimensions, Phys. Rev. E 57 (1998) 4323–4349. http://dx.doi.org/10.1103/PhysRevE.57.4323.

[18] N.A. Ahmad, A.A. Wheeler, W.J. Boettinger, G.B. McFadden, Solute trapping and solute drag in a phase-field model of rapid solidification, Phys. Rev. E 58 (1998) 3436–3450. http://dx.doi.org/10.1103/PhysRevE.58.3436.

[19] P.G. Sanders, M.J. Aziz, Self-diffusivity of liquid silicon measured by pulsed laser melting, J. Appl. Phys. 86 (8).

[20] M.J. Aziz, Model for solute redistribution during rapid solidification, J. Appl. Phys. 53 (2).

[21] J. Narayan, C.W. White, M.J. Aziz, B. Stritzker, A. Walthuis, Pulsed excimer (krf) laser melting of amorphous and crystalline silicon layers, J. Appl. Phys. 57 (2).
[22] M.J. Aziz, J.Y. Tsao, M.O. Thompson, P.S. Peercy, C.W. White, Solute trapping: comparison of theory with experiment, Phys. Rev. Lett. 56 (1986) 2489–2492. http://dx.doi.org/10.1103/PhysRevLett.56.2489.
[23] J.Y. Tsao, M.J. Aziz, M.O. Thompson, P.S. Peercy, Asymmetric melting and freezing kinetics in silicon, Phys. Rev. Lett. 56 (1986) 2712–2715. http://dx.doi.org/10.1103/PhysRevLett.56.2712.
[24] W. Boettinger, M. Aziz, Theory for the trapping of disorder and solute in intermetallic phases by rapid solidification, Acta Metall. 37 (12) (1989) 3379–3391. http://dx.doi.org/10.1016/0001-6160(89)90210-1 (URL ⟨http://www.sciencedirect.com/science/article/pii/0001616089902101⟩).
[25] J. Kittl, P. Sanders, M. Aziz, D. Brunco, M. Thompson, Complete experimental test of kinetic models for rapid alloy solidification, Acta Mater. 48 (20) (2000) 4797–4811. http://dx.doi.org/10.1016/S1359-6454(00)00276-7 (URL ⟨http://www.sciencedirect.com/science/article/pii/S1359645400002767⟩).
[26] K.A. Jackson, G.H. Gilmer, D.E. Temkin, Monte carlo simulation of the rapid crystallization of bismuth-doped silicon, Phys. Rev. Lett. 75 (1995) 2530–2533. http://dx.doi.org/10.1103/PhysRevLett.75.2530.
[27] D.L. Woodraska, J.A. Jaszczak, A monte carlo simulation method for 111 surfaces of silicon and other diamond-cubic materials, Surf. Sci. 374 (1) (1997) 319–332. http://dx.doi.org/10.1016/S0039-6028(96)01201-0 (URL ⟨http://www.sciencedirect.com/science/article/pii/S0039602896012010⟩).
[28] S. Stiffler, P. Evans, A. Greer, Interfacial transport kinetics during the solidification of silicon, Acta Metall. Et. Mater. 40 (7) (1992) 1617–1622. http://dx.doi.org/10.1016/0956-7151(92)90103-L (URL ⟨http://www.sciencedirect.com/science/article/pii/095671519290103L⟩).
[29] K. Beatty, K. Jackson, American crystal growth 1996 and vapor growth and epitaxy 1996 orientation dependence of the distribution coefficient obtained from a spin-1 ising model, J. Cryst. Growth 174 (1) (1997) 28–34. http://dx.doi.org/10.1016/S0022-0248(96)01057-3 (URL ⟨http://www.sciencedirect.com/science/article/pii/S0022024896010573⟩).
[30] P.M. Fahey, P.B. Griffin, J.D. Plummer, Point defects and dopant diffusion in silicon, Rev. Mod. Phys. 61 (1989) 289–384. http://dx.doi.org/10.1103/RevModPhys.61.289.
[31] H. Kodera, Diffusion coefficients of impurities in silicon melt, Jpn. J. Appl. Phys. 2 (4) (1963) 212–219. http://dx.doi.org/10.1143/JJAP.2.212 (URL ⟨http://jjap.jsap.jp/link?JJAP/2/212/⟩).
[32] E.V. Monakhov, B.G. Svensson, M.K. Linnarsson, A. La Magna, M. Italia, V. Privitera, G. Fortunato, M. Cuscun, L. Mariucci, The effect of excimer laser pretreatment on diffusion and activation of boron implanted in silicon, Appl. Phys. Lett. 87 (19). http://dx.doi.org/10.1063/1.2126144 URL ⟨http://scitation.aip.org/content/aip/journal/apl/87/19/10.1063/1.2126144⟩
[33] K.K. Ong, K.L. Pey, P.S. Lee, A.T. S. Wee, X.C. Wang, Y.F. Chong, Dopant distribution in the recrystallization transient at the maximum melt depth induced by laser annealing, Appl. Phys. Lett. 89 (17). http://dx.doi.org/10.1063/1.2364834 URL ⟨http://scitation.aip.org/content/aip/journal/apl/89/17/10.1063/1.2364834⟩
[34] M. Hackenberg, K. Huet, R. Negru, J. Venturini, G. Fisicaro, A. La Magna, P. Pichler, Modeling boron profiles in silicon after pulsed excimer laser annealing, in: AIP Conference Proceedings 1496 (1) (2012) 241–244. http://dx.doi.org/10.1063/1.4766533 URL ⟨http://link.aip.org/link/?APC/1496/241/1⟩
[35] T. Kaplan, M.J. Aziz, L.J. Gray, Application of onsagers reciprocity relations to interface motion during phase transformations, J. Chem. Phys. 90 (2).
[36] M.J. Aziz, Dissipationtheory treatment of the transition from diffusioncontrolled to diffusionless solidification, Appl. Phys. Lett. 43 (6).
[37] L. Onsager, Reciprocal relations in irreversible processes. I, Phys. Rev. 37 (1931) 405–426. http://dx.doi.org/10.1103/PhysRev.37.405.
[38] L. Onsager, Reciprocal relations in irreversible processes. II, Phys. Rev. 38 (1931) 2265–2279. http://dx.doi.org/10.1103/PhysRev.38.2265.
[39] I. Štich, R. Car, M. Parrinello, Bonding and disorder in liquid silicon, Phys. Rev. Lett. 63 (1989) 2240–2243. http://dx.doi.org/10.1103/PhysRevLett.63.2240.
[40] J.T. Okada, P.H.-L. Sit, Y. Watanabe, Y.J. Wang, B. Barbiellini, T. Ishikawa, M. Itou, Y. Sakurai, A. Bansil, R. Ishikawa, M. Hamaishi, T. Masaki, P.-F. Paradis, K. Kimura, T. Ishikawa, S. Nanao, Persistence of covalent bonding in liquid silicon probed by inelastic x-ray scattering, Phys. Rev. Lett. 108 (2012) 067402. http://dx.doi.org/10.1103/PhysRevLett.108.067402.
[41] N. Jakse, A. Pasturel, Dynamics of liquid and undercooled silicon: an ab initio molecular dynamics study, Phys. Rev. B 79 (2009) 144206. http://dx.doi.org/10.1103/PhysRevB.79.144206.
[42] P.A. Stolk, H.-J. Gossmann, D.J. Eaglesham, D.C. Jacobson, C.S. Rafferty, G.H. Gilmer, M. Jaraz, J.M. Poate, H.S. Luftman, T.E. Haynes, physics mechanism transient enhanced dopant diffusion in ion-implanted silicon, J. Appl. Phys. 81 (9).
[43] L. Pelaz, L.A. Marqus, M. Aboy, P. Lpez, I. Santos, Front-end process modeling in silicon, Eur. Phys. J. B 72 (3) (2009) 323–359. http://dx.doi.org/10.1140/epjb/e2009-00378-9.
[44] M. Jaraiz, G.H. Gilmer, J.M. Poate, T.D. de la Rubia, Atomistic calculations of ion implantation in si: Point defect and transient enhanced diffusion phenomena, Appl. Phys. Lett. 68 (3).
[45] L. Pelaz, M. Jaraiz, G.H. Gilmer, H.-J. Gossmann, C.S. Rafferty, D.J. Eaglesham, J. M. Poate, B diffusion and clustering in ion implanted si: the role of b cluster precursors, Appl. Phys. Lett. 70 (17).
[46] G. Fisicaro, L. Pelaz, M. Aboy, P. Lopez, M. Italia, K. Huet, F. Cristiano, Z. Essa, Q. Yang, E. Bedel-Pereira, M. Quillec, A.L. Magna, Kinetic monte carlo simulations of boron activation in implanted si under laser thermal annealing, Appl. Phys. Express 7 (2) (2014) 021301 (URL ⟨http://stacks.iop.org/1882-0786/7/i=2/a=021301⟩).
[47] M. Aboy, L. Pelaz, E. Bruno, S. Mirabella, S. Boninelli, Kinetics of large b clusters in crystalline and preamorphized silicon, Journal of Applied Physics 110 (7). http://dx.doi.org/10.1063/1.3639280 URL ⟨http://scitation.aip.org/content/aip/journal/jap/110/7/10.1063/1.3639280⟩
[48] R. Falster, V. Voronkov, F. Quast, On the properties of the intrinsic point defects in silicon: A perspective from crystal growth and wafer processing, physica status solidi (b) 222 (1) (2000) 219–244. http://dx.doi.org/10.1002/1521–3951/200011/222:1219::AID-PSSB2193.0.CO;2-U
[49] N.E.B. Cowern, G. Mannino, P.A. Stolk, F. Roozeboom, H.G.A. Huizing, J.G.M. van Berkum, F. Cristiano, A. Claverie, M. Jaraíz, Energetics of self-interstitial clusters in si, Phys. Rev. Lett. 82 (1999) 4460–4463. http://dx.doi.org/10.1103/PhysRevLett.82.4460.
[50] F. Cristiano, J. Grisolia, B. Colombeau, M. Omri, B. de Mauduit, A. Claverie, L.F. Giles, N.E.B. Cowern, Formation energies and relative stability of perfect and faulted dislocation loops in silicon, J. Appl. Phys. 87 (12).
[51] A. Bongiorno, L. Colombo, T.D.D. la Rubia, Structural and binding properties of vacancy clusters in silicon, EPL (Europhys. Lett.) 43 (6) (1998) 695 (URL ⟨http://stacks.iop.org/0295-5075/43/i=6/a=695⟩).
[52] G. Fisicaro, M. Italia, V. Privitera, G. Piccitto, K. Huet, J. Venturini, A. La Magna, Dopant activation and damage evolution in implanted silicon after excimer laser annealing, Phys. Status Solidi (c) 8 (3) (2011) 940–943. http://dx.doi.org/10.1002/pssc.201000252
[53] A.L. Magna, S. Coffa, S. Libertino, L. Brambilla, P. Alippi, L. Colombo, A multi-scale atomistic study of the interstitials agglomeration in crystalline si, Nucl. Instrum. Methods Phys. Res. Sect. B: Beam Interact. Materials Atoms 178 (14) (2001) 154 – 159, materials Science with Ion Beams. http://dx.doi.org/10.1016/S0168-583X(01)00502-X URL ⟨http://www.sciencedirect.com/science/article/pii/S0168583×0100502X⟩
[54] L. Marques, Manuscript in Preparation.